Available online at www.sciencedirect.com

SCIENCE DIRECT®

International Journal of Heat and Fluid Flow 25 (2004) 44–57

International Journal of HEAT AND FLUID FLOW

www.elsevier.com/locate/ijhff

Interfacial structures in confined cap-turbulent and churn-turbulent flows

Xiaodong Sun [a,*], Seungjin Kim [a], Ling Cheng [a], Mamoru Ishii [a], Stephen G. Beus [b]

[a] *Thermal-Hydraulics and Reactor Safety Laboratory, School of Nuclear Engineering, Purdue University, 400 Central Drive, West Lafayette, IN 47907-2017, USA*

[b] *Bettis Atomic Power Laboratory, Bechtel Bettis, Inc., Post Office Box 79, West Mifflin, PA 15122-0079, USA*

Received 14 February 2003; accepted 20 August 2003

Abstract

The objective of the present work is to study and model the interfacial structure development of air–water two-phase flow in a confined flow passage. Experiments of a total of 13 flow conditions in cap-turbulent and churn-turbulent flow regimes are carried out in a vertical air–water upward two-phase flow experimental loop with a test section of 200 mm in width and 10 mm in gap. Miniaturized four-sensor conductivity probes are used to measure local two-phase parameters at three different elevations for each flow condition. Bubble characteristics captured by the probes are categorized into two groups in view of the two-group interfacial area transport equation, i.e., spherical/distorted bubbles as Group 1 and cap/churn-turbulent bubbles as Group 2. The acquired local parameters are time-averaged void fraction, interfacial velocity, bubble number frequency, interfacial area concentration, and bubble Sauter mean diameter for each group of bubbles. Also, the line-averaged and area-averaged data are presented and discussed in detail. The comparisons of these parameters at different elevations demonstrate the development of interfacial structures along the flow direction due to bubble interactions and the hydrodynamic effects. Furthermore, these data can serve as one part of the experimental data for investigation of the interfacial area transport in a confined two-phase flow.

Keywords: Interfacial structures; Interfacial area; Local measurement; Cap-turbulent flow; Churn-turbulent flow; Conductivity probe

---

1. Introduction

In gas–liquid two-phase flow, the void fraction and interfacial area concentration characterize the geometric capability of the interfacial transfer of mass, momentum, and energy between the two phases. Historically, flow regime-dependent correlations have been used to determine the interfacial area concentration in nuclear reactor thermal-hydraulics and safety system analysis codes. Most of the flow regime transition criteria were developed for static fully developed flow (Mishima and Ishii, 1984; Ishii, 1987). However, in most industrial applications, fully developed two-phase flow may not always be achieved due to the interactions of fluid particles and finite length of flow passages. Therefore, this correlation approach does not properly account for either the dynamic nature of the development in the interfacial structures or the entrance effects of the flow. In view of this, Kocamustafaogullari and Ishii (1995) proposed a dynamic and mechanistic approach, namely, the interfacial area transport equation. By mechanistically modeling the major bubble coalescence and disintegration phenomena, Wu et al. (1998b) and Kim et al. (2001b) developed the one-group interfacial area transport equation, which is applicable to bubbly flow. In conjunction with the theoretical efforts, experimental study was performed to acquire interfacial structure data in bubbly flow (Kim et al., 2001a).

In cap-turbulent, slug, and churn-turbulent flow, there exist bubbles of different size and shape, such as spherical, distorted, cap, slug, and churn-turbulent bubbles. The differences in bubble size and shape lead to substantial differences in bubble transport phenomena, such as drag force, bubble interaction mechanisms, etc.

---

[*] Corresponding author. Tel.: +1-765-494-5759; fax: +1-765-494-9570.

E-mail address: xsun@ecn.purdue.edu (X. Sun).

0142-727X/$ - see front matter © 2003 Elsevier Inc. All rights reserved.
doi:10.1016/j.ijheatfluidflow.2003.08.001

Nomenclature

a_{i}	interfacial area concentration (1/m)
$D_{\mathrm{d,max}}$	maximum size of distorted bubbles (m)
D_{h}	hydraulic diameter of test section (m)
D_{sm}	Sauter mean diameter of bubbles (m)
f_{b}	bubble number frequency (1/s)
G	gap of test section (m)
g	gravitational acceleration (m/s^2)
j	volumetric flux (superficial velocity) (m/s)
$\vec{n}$	unit outward normal vector of interface
s_{0k}	spacing between sensor 0 and sensor k for a conductivity probe (m)
$\vec{v}$, v	velocity (m/s)
x	coordinate in width direction
y	coordinate in gap direction
z	coordinate in vertical (axial) direction

Greeks

α	void fraction
σ	surface tension (N/m)
$\Delta\rho$	density difference between two phases (kg/m^3)
ΔT	time interval (s)
Δt_{kj}	time delay of the signals between sensors 0 and k for the jth interface (s)

Subscripts

0	gas property at standard condition
1	Group 1 bubbles
2	Group 2 bubbles
f	liquid phase
g	gas phase
i	interface
x	distribution in x-direction
z	z-direction

Superscript

t	time

Mathematical symbols

$\bar{\ }$	averaging
$\langle\ \rangle$	area averaging
$\ll\ \gg$	void-weighted area averaging

In the one-group interfacial area transport equation, which only focuses on small bubbles, these differences have not been accounted for due to its one-group nature (Wu et al., 1998b; Kim et al., 2001b). Therefore, to describe the development of the interfacial structures in a more generalized two-phase flow, the one-group transport equation needs to be extended to a multi-group transport equation. For simplicity, a two-group transport equation appears practical and reasonable (Wu et al., 1998a). To evaluate the two-group transport equation a reliable database is indispensable.

The present study is a continuation of the previous experimental efforts for bubbly flow (Kim et al., 2001a). Extensive experiments have been carried out in the same upward air–water experimental loop to establish a reliable database, as well as to gain a better understanding for the development of the interfacial structures for cap-turbulent and churn-turbulent flow. A database in 13 flow conditions at cap-turbulent and churn-turbulent flow regimes is obtained by using miniaturized four-sensor conductivity probes, which is the state-of-the-art for local interfacial measurements (Kim et al., 2000). The measured parameters are local void fraction, interfacial velocity, and bubble number frequency for both Group 1 and Group 2 bubbles at three different elevations. Here, Group 1 bubbles include spherical and distorted bubbles while Group 2 bubbles are cap-turbulent and churn-turbulent bubbles since no stable slug bubbles were observed during the experiments. The churn-turbulent bubbles refer to highly distorted cap bubbles and very chaotic large bubbles (Taitel et al., 1980). Then, the local interfacial area concentration and bubble Sauter mean diameter can also be obtained for both groups of bubbles based on the above measured parameters. The comparisons of these parameters at different elevations demonstrate the development of interfacial structures along the flow direction. The underlying physical mechanisms of this development, i.e., bubble coalescence and disintegration, and the hydrodynamic effects, are also identified and discussed in detail.

2. Measurement technique for multi-sensor conductivity probe

The conductivity probe, first proposed by Neal and Bankoff (1963), is based on the fundamental differences in electrical conductivity between the two phases, i.e., water and air in this study. It has been one of the most widely used measurement techniques in gas–liquid two-phase flow experiments due to its capability of measuring local two-phase parameters (Hewitt, 1978; Kataoka et al., 1986; Kataoka and Serizawa, 1990; Revankar and Ishii, 1992; Kalkach-Navarro et al., 1993; Kocamustafaogullari et al., 1994; Kim et al., 2000). The characteristic rise/fall of the impedance signals (converted to voltage signals through an electric circuit) between the sensors and common ground can be obtained as the bubbles pass through the exposed tips of the probe sensors. Therefore, the local time-averaged void fraction can be obtained by dividing the sum of the time occupied by the gas-phase by the total measurement time. The most important feature of the conductivity probe is its capability of measuring the local interfacial velocity of bubbles with multiple sensors, by which the local time-averaged interfacial area concentration can be calculated (Kataoka et al., 1986). Based on the scope of the present experimental study and the necessity of acquiring local two-phase parameters, the multi-sensor conductivity probe is chosen as the local instrument in the experiments.

The measurement principle of the multi-sensor conductivity probe for the local time-averaged interfacial area concentration ($\bar{a}_{\mathrm{i}}^{t}$) is based on the relation between the interfacial area concentration and interfacial velocity given by Ishii (1975) as,

$$\bar{a}_{\mathrm{i}}^{t} = \frac{1}{\Delta T}\sum_{j}\left(\frac{1}{|\vec{v}_{\mathrm{i}}\cdot\vec{n}_{\mathrm{i}}|}\right)_{j}, \tag{1}$$

where j represents the jth interface which passes a local point during the time interval ΔT. Here, $\vec{v}_{\mathrm{i}}$ and $\vec{n}_{\mathrm{i}}$ are the bubble interfacial velocity and unit outward normal vector of the jth interface, respectively. Eq. (1) implies that the local interfacial area concentration can be obtained if the bubble interfacial velocity is known.

In view of Eq. (1), Kataoka et al. (1986) formulated a mathematical expression to determine the local time-averaged interfacial area concentration for both double-sensor and four-sensor probes. For the double-sensor probe, it is necessary to make certain statistical assumptions on bubble parameters, such as spherical in shape, etc. Consequently, the application of the double-sensor probe becomes limited in the flow conditions where the shapes of bubbles vary significantly from spherical, such as cap, slug, and/or churn-turbulent bubbles. This led to the development of the four-sensor conductivity probe.

In the four-sensor conductivity probe, three pairs of double-sensor probes can be formed with one common sensor in the upstream and three independent sensors in the downstream. Therefore, given the spacing between the probe sensors, three components of the interfacial velocity can be obtained at a local point for each interface by measuring the time delay between the signals from three pairs of double-sensors, such as

$$v_{kj} = \frac{s_{0k}}{\Delta t_{kj}}, \tag{2}$$

if the sensor spacing s_{0k} ($k = 1$, 2, and 3) is relatively small. Here, Δt_{kj} is the time delay of the signals between sensors 0 and k for the jth interface; and v_{kj} is the measured velocity value in k-direction of jth interface.

When the directions of the three independent probes are chosen as the x, y, and z-axes, Kataoka et al. (1986) proposed the following formulation for a four-sensor conductivity probe

$$\bar{a}_{\mathrm{i}}^{t}(\vec{x}_o) = \frac{1}{\Delta T}\sum_{j}\left[\left(\frac{1}{v_{1j}}\right)^2 + \left(\frac{1}{v_{2j}}\right)^2 + \left(\frac{1}{v_{3j}}\right)^2\right]^{1/2}. \tag{3}$$

However, in general, the directional cosines of each sensor with respect to the space coordinates will be involved in calculating the time-averaged interfacial area for non-spherical bubbles, as presented by Fu (2001). On the other hand, the void fraction of Group 2 bubbles, α_2, are determined as the ratio of the sum of the time occupied by the Group 2 bubbles to the total measurement time. Then, the size of Group 2 bubbles is obtained in terms of the Sauter mean diameter as

$$D_{\mathrm{sm}k} = 6\alpha_k/a_{\mathrm{i}k}, \tag{4}$$

where, $k = 1$ or 2 for Group 1 and Group 2 bubbles, respectively. It is clear that in the applications of the four-sensor probe, unlike the double-sensor probe technique, no hypothesis for the bubble shape is necessary in the mathematical formulation to calculate the local interfacial area concentration.

However, in the application of the four-sensor conductivity probe, difficulties were reported by previous studies (Revankar and Ishii, 1992). The limitations were mainly caused by the size of the probe and its geometric configuration. The large measurement area and the large spacing between the sensors caused a significant number of bubbles to miss some of the sensors. It was also reported that the deformation of the bubble surface could be significant as the bubble was penetrated by the sensors.

Recently, Kim et al. (2000) significantly improved the geometric configurations of the probe. The four-sensor conductivity probe was miniaturized and therefore, its capability was extensively enhanced. The newly designed four-sensor conductivity probe consists of one common sensor, which is in the front of the probe, and three rear sensors. One of the three rear sensors is arranged in such a way that it is just beside the common sensor, i.e., this rear sensor and the common sensor can be considered a double-sensor probe that measures interfacial velocity in the flow direction since the line between the tips of these two sensors are made parallel with the flow. The cross-sectional measurement area of the miniaturized four-sensor probe is significantly reduced. This can effectively minimize both the number of missing bubbles and the deformation of passing bubble interfaces. Therefore, the newly designed four-sensor probe can be utilized in a wide range of two-phase flow regimes spanning over bubbly, cap, slug, and churn-turbulent flows. Moreover, it allows one to identify and separate the local parameters into two groups of bubbles and to observe how they develop along the flow field even when the flow regime transition occurs.

In addition to the improvements of the design and fabrication of the four-sensor conductivity probe, the signal processing scheme was also significantly upgraded to accommodate the newly designed probe (Kim et al., 2000). The signal processing includes noise filtering, signal normalization, square signal conversion, bubble categorization, parameters calculation, and correction processes. First, a simple DC circuit is employed in the experiments to convert the impedance signals to the voltage signals. The circuit outputs a high voltage when the sensor tip is in the gas phase, vice versa. A moving median filter is applied to remove high frequency random noises. Then, the signals are normalized using the maximum and minimum voltage values, and the square signals are generated by setting a threshold value of 0.05, i.e., a bubble interface is considered to encounter the sensor tip when the normalized signal is larger than 0.05.

After the signal conditioning process is completed, the interfacial velocity is approximately estimated and the signals are further categorized and separated into those of Group 1 and Group 2 bubbles. For the current experiment, the cap and churn-turbulent bubbles are essentially two dimensional in terms of shape and motion. Theoretically, it may be required to have two length scales to characterize the cap and churn-turbulent bubbles, such as the chord length and the length in the transverse direction (width-direction). However, for the current local conductivity probe, due to the localization of the information, it would be extremely difficult to instantaneously retrieve global information for the bubbles beyond where the sensors are located (Fu, 2001). On the other hand, in the cap-turbulent and churn-turbulent regimes, large bubbles, i.e., cap and churn-turbulent bubbles, have relatively large size, both in the main flow direction and the transverse direction; while the small bubbles, i.e., the spherical and distorted bubbles, are usually less than 6 mm in the current air–water atmospheric pressure condition. Therefore, in the bubble categorization process, a single-length scale criterion may be acceptable, in particular for the current confined flows. Therefore, the maximum size of distorted bubbles, $D_{\mathrm{d,max}}$, is used as the criterion of group boundary in identifying bubble types. The bubbles with a chord length smaller than $D_{\mathrm{d,max}}$ are categorized as Group 1 bubbles, otherwise are Group 2. Here $D_{\mathrm{d,max}}$ is given by Kocamustafaogullari et al. (1984) as

$$D_{\mathrm{d,max}} = 4\sqrt{\sigma/g\Delta\rho}, \tag{5}$$

which is approximately 10 mm for air–water flow under atmospheric pressure condition.

It should be noted, however, this approach to distinguish bubble groups could result in errors, in particular at the edge of a cap bubble where the chord length is less than the maximum distorted bubble length, given by Eq. (5). In this case, the bubble frequency as well as the void fraction and interfacial area concentration in Group 2 bubbles will be underestimated. The errors that may result owing to the uncertainties in identifying the two groups of bubbles strongly depend on the flow conditions, i.e., the void fraction and bubble size, etc. The error will be relatively smaller if the average size of Group 2 bubbles is large. To minimize the errors, Fu (2001) provided one correction scheme to compensate the miss-counted bubble number as well as the void fraction and interfacial area concentration. The scheme has been incorporated in the signal processing program.

After the bubble categorization, the local time-averaged two-phase parameters, such as bubble frequency, interfacial velocity, void fraction, interfacial area concentration, and Sauter mean diameter of each group of bubbles, are obtained. The calculation process is based on the formulations discussed earlier, however, the missing bubbles and the non-effective signals are carefully accounted for, as discussed by Kim et al. (2000) in detail.

To benchmark the newly developed conductivity probe and its signal processing scheme, an image analysis was employed (Kim et al., 2000). In the benchmark study, images captured in a bubbly flow and a slug flow were analyzed. For the bubbly flow, experiments were performed in an acrylic vertical rectangular flow channel. A computer code was used to process the captured images to obtain the location and the size of each bubble in a given image frame; then the line-averaged (over the depth direction of the flow channel) void fraction and interfacial area concentration were calculated. On the other hand, images in the slug flow were captured in a round pipe; and only the images of Taylor bubbles were analyzed and compared to the results by the four-sensor conductivity probe. In the image processing of Taylor bubbles, the contour of Taylor bubbles was calculated with respect to the slug length by assuming symmetric front and flat rear interfaces. The two comparisons showed that the relative percentage difference between the four-sensor conductivity probe and the image analysis was within ±10%. From the benchmark experiments, therefore, it was assumed that 10% measurement uncertainty was expected in the current experiments.

3. Experiments

3.1. Experimental facility

The present study is an extension of the previous work performed by Kim et al. (2001a) and therefore, the same experimental facility is used. Fig. 1 shows a schematic diagram of the experimental facility. The experimental facility includes a two-phase mixing section, a test section, an upper plenum, a water reservoir, water and air delivery systems, and instrumentation. The loop is operated under atmospheric pressure. The de-mineralized

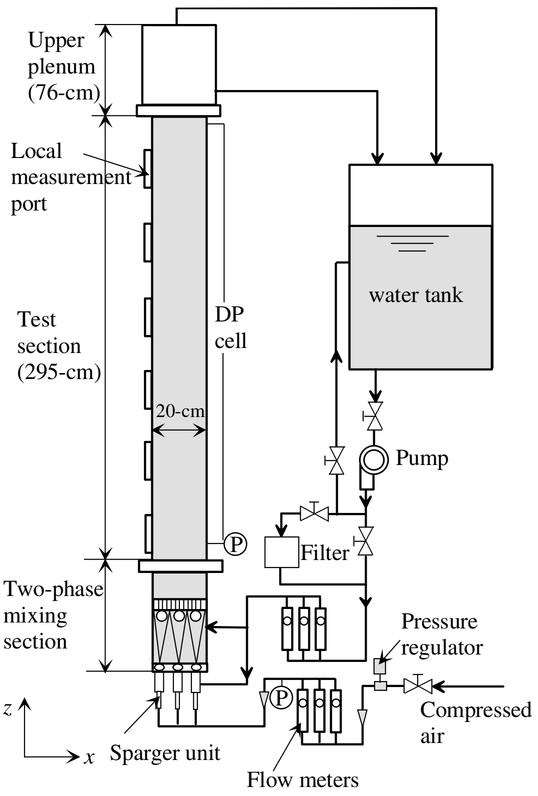

Fig. 1. Schematic of the experimental loop.

Table 1
Experimental conditions

Run no.	j_f [m/s]	j_{g0}[a] [m/s]	Local j_g [m/s]		
			Port 2	Port 4	Port 6
8	1.89	0.39	0.29	0.32	0.36
10	0.32	0.41	0.34	0.36	0.38
11	0.95	0.47	0.37	0.40	0.43
12	2.84	1.00	0.73	0.82	0.93
13	2.84	2.01	1.43	1.61	1.84
14	0.63	0.42	0.34	0.36	0.39
15	1.89	0.58	0.44	0.48	0.53
16	1.26	0.66	0.52	0.56	0.61
17	1.40	0.52	0.41	0.44	0.48
18	0.95	0.94	0.77	0.82	0.88
19	1.89	0.97	0.75	0.82	0.90
20	0.95	1.88	1.56	1.67	1.79
21	1.89	1.95	1.52	1.66	1.83

[a] This gas superficial velocity is converted to the standard condition (1.0133×10^5 Pa pressure and 293 K temperature).

water is supplied by a centrifugal pump while the air is delivered by an air compressor. For the measurement of air volumetric flow rate, several rotameters together with a precise pressure gauge are used. The rotameters have an accuracy of ±2% full-scale (FS) reading, while the pressure gauge has a ±1% FS reading accuracy. For the liquid flow rate, rotameters with the same accuracy are installed for low flow rates. In addition, two vortex flow meters with ±2% FS accuracy are installed to measure large liquid flow rates. At the inlet of the test section, a precise pressure gauge with ±1% FS accuracy is installed to measure the inlet pressure. Also, a differential pressure (DP) cell with a ±1% FS accuracy is mounted between the inlet and the exit of the test section to measure the pressure drop along the test section.

The current test section is 200 mm in width (x-direction) and 10 mm in gap (y-direction). It is made of clear acrylic material and has great advantages for flow visualization due to the following facts: the motion of the air-bubbles is close to two dimensional; the influence of the overlap of the bubbles on the image analysis is minimized; and the image distortion due to curvature effect is eliminated. Six local measurement ports are installed in the gap side along the test section. The z/D_h values from Port 1 to Port 6 are 8.0, 34.8, 61.5, 88.2, 115.0, and 141.7, respectively. At each port, a conductivity probe can be traversed in both directions in the cross section of the test section to obtain local measurement data.

The air–water two-phase mixture is generated by a specially designed two-phase mixing apparatus. Six porous sparger units are installed, three on each side of the duct-width, to generate bubbles of near-uniform size. These sparger units are arranged in equal spacing relative to each other to minimize artificial bubble interactions at the outlet of the bubble injection apparatus. The porous surface area of each sparger is 17.5 cm^2 with average pore size of 10 μm. The total liquid flow rate is achieved by two liquid injections: one through the annulus of the six sparger units in the bubble injection apparatus to shear bubbles off from the sparger tube surfaces and another through the three main liquid lines located on the front side of the lower part of the bubble injection apparatus.

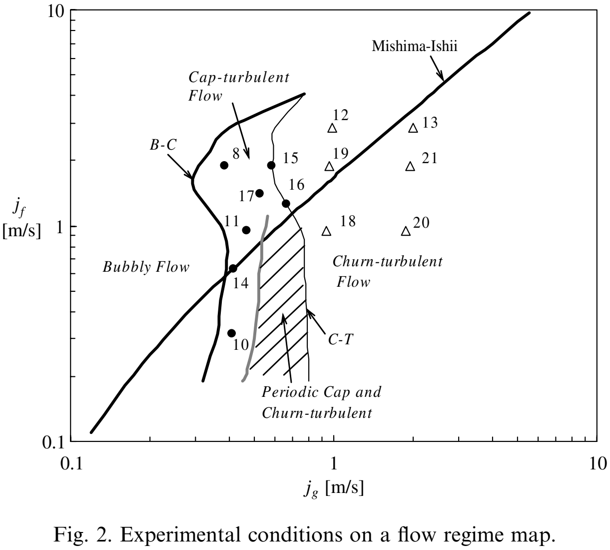

Fig. 2. Experimental conditions on a flow regime map.

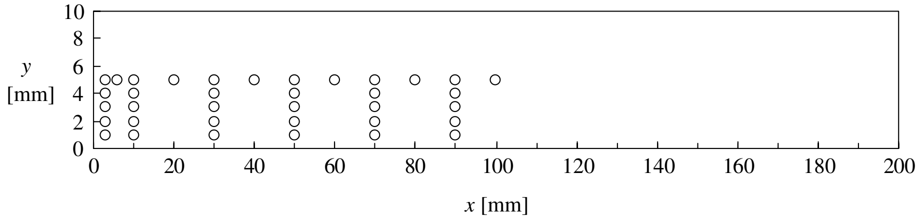

Fig. 3. Measurement points at each axial measurement port.

3.2. Experimental conditions

In the present study, experiments of seven cap-turbulent and six churn-turbulent flow conditions have been carried out. Table 1 shows the flow conditions in detail and Fig. 2 presents them on a flow regime map. In the table, to obtain local j_g values at different measurement ports, the ideal gas law is assumed valid and the local pressure is determined by linear interpolation of the pressure drop measured by the DP cell. In Fig. 2, the transition line from bubbly to slug flow identified by Mishima and Ishii (1984) was developed for round pipes. The other two transition lines were identified based on the current experimental test section by flow visualization. B–C and C–T denote transitions from bubbly to cap-turbulent and cap-turbulent to churn-turbulent flows, respectively. The flow regime investigation showed that a periodic unstable cap-turbulent

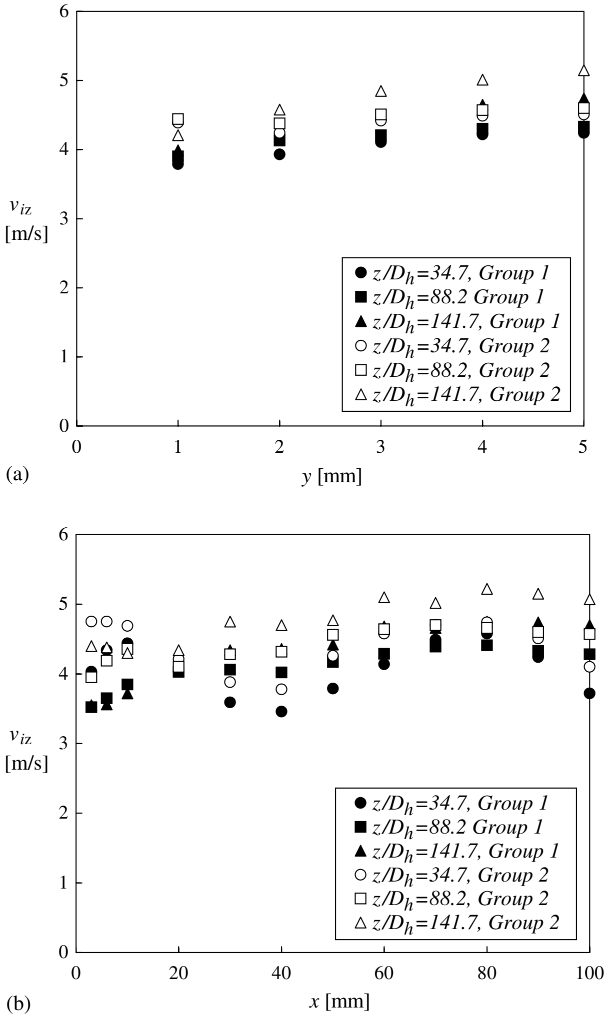

Fig. 4. Interfacial velocity of both groups of bubbles at (a) center region in width direction ($x = 90$ mm) and (b) centerline in gap direction ($y = 5$ mm) for Run 12 at three elevations.

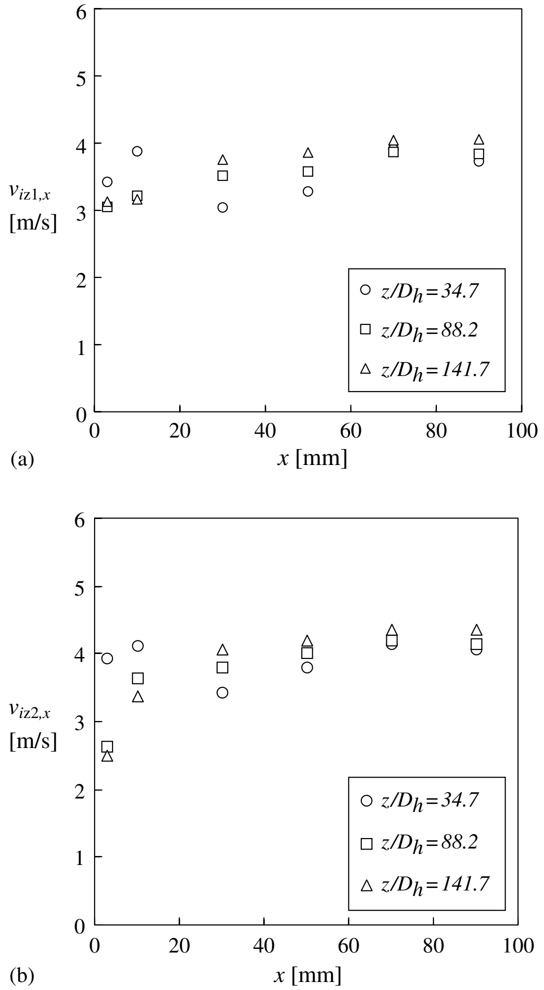

Fig. 5. y-Direction line-averaged bubble velocity of (a) Group 1 and (b) Group 2 bubbles for Run 12 at three elevations.

and churn-turbulent region exists at low liquid flow rates (Kim et al., 2001a). Also, in this region, due to the strong wake effect of cap or churn-turbulent bubbles in relatively low liquid flows, noticeable local flow re-circulation occurs behind cap or churn-turbulent bubbles. In addition, at low liquid flow rates, the re-circulation phenomenon can be observed in churn-turbulent flow regime close to the transition of cap-turbulent to churn-turbulent flows. Since the re-circulation phenomenon can greatly hamper the measurement accuracy of the four-sensor conductivity probe, the current flow conditions are chosen to avoid the local flow re-circulation region.

For most flow conditions, the local measurements are performed at Ports 2, 4, and 6, which correspond to z/D_h values of 34.8, 88.2, and 141.7, respectively. However, for Runs 18–21, data only at Ports 2 and 6 are collected. At each measurement port, measurements at a total of 36 points are made in a quarter of the cross sectional area of the test section, as shown in Fig. 3. Spot check is done to assure good symmetry of the flow before actual data acquisition takes place. To obtain good statistical results, at least 1000 Group 1 and 200 Group 2 bubbles are acquired at most measurement points (no or few Group 2 bubbles are observed in some measurement points for certain flow conditions) by adjusting the data acquisition time. The data acquisition frequency varies from 8000 to 30,000 Hz depending on flow condition.

It should be noted that in the previous experiments performed for bubbly flow, Run 8 is actually in cap-turbulent flow regimes (Kim et al., 2001a). However, due to the low number frequency of Group 2 bubbles as well as the available measurement technique, the

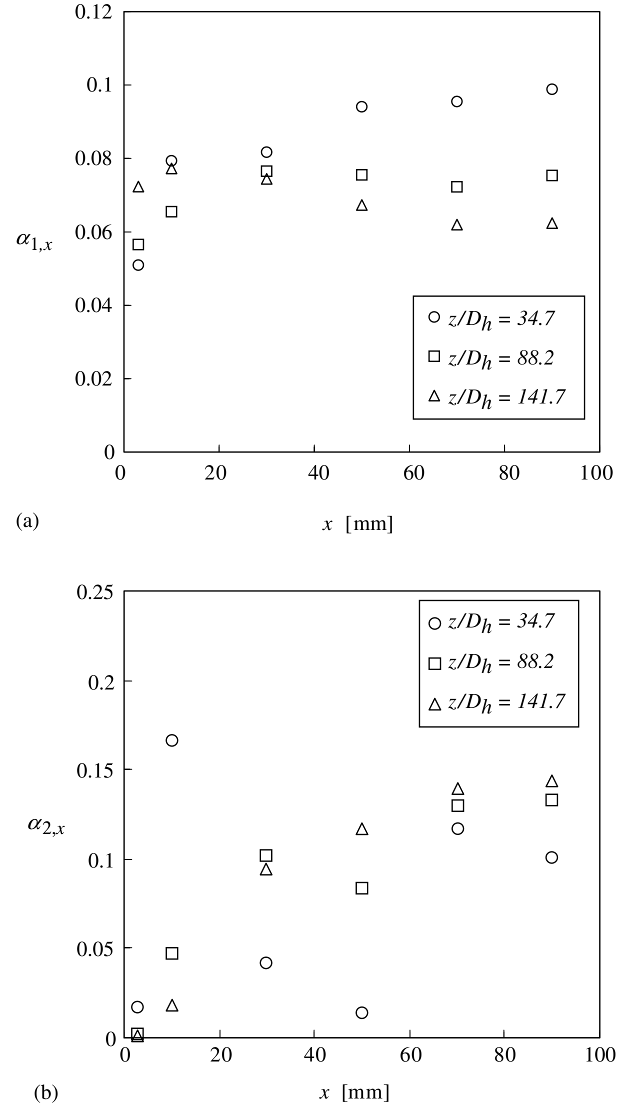

Fig. 6. *y*-Direction line-averaged void fraction of (a) Group 1 and (b) Group 2 bubbles for Run 12 at three elevations.

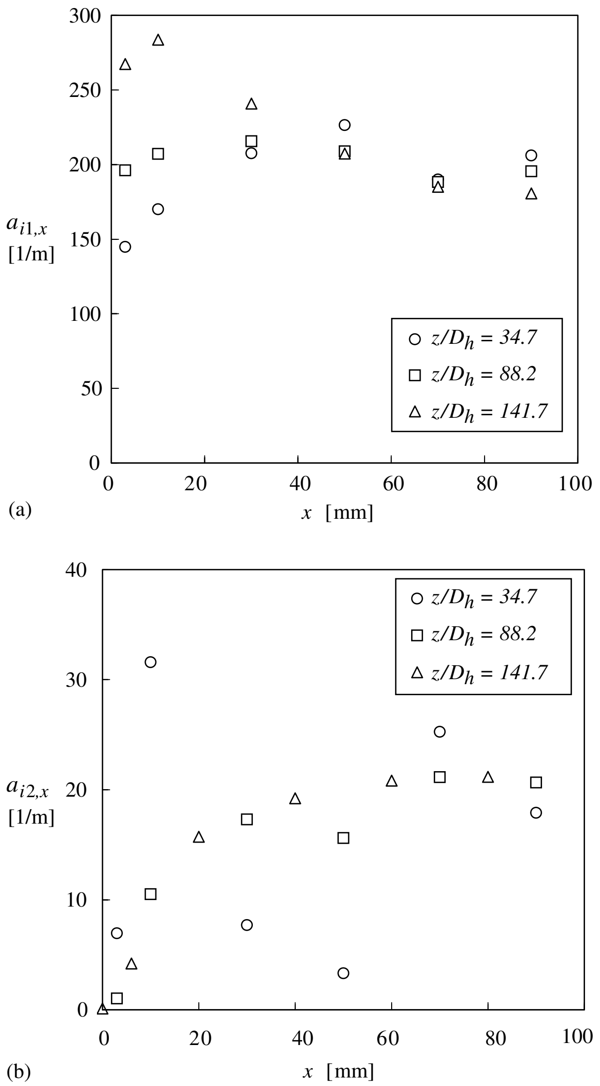

Fig. 7. *y*-Direction line-averaged interfacial area concentration of (a) Group 1 and (b) Group 2 bubbles for Run 12 at three elevations.

double-sensor conductivity probe, which is applicable to bubbly flow, was used as local instrument. In the current study, a four-sensor probe is used and the data in this flow condition is re-acquired.

4. Results and discussions

Characteristic local and line-averaged measurement results are first presented and discussed. Then, the development of flow structures is examined by comparing the profiles of the line-averaged and area-averaged two-phase parameters at various measurement elevations. The important bubble interaction mechanisms and the hydrodynamic effects on the development of interfacial structures are identified.

Shown first in Fig. 4 are the local profiles of axial (z-direction) interfacial velocities of Group 1 and Group 2 bubbles at three different elevations for Run 12. They are measured at the centerline (or center region) of both the width and gap directions. Run 12, in which j_{f} and j_{g0} are 2.84 and 1.00 m/s, respectively, is in churn-turbulent flow regime. In general, the axial interfacial velocity distributions for both groups in y-direction at $x = 90$ mm show a quite flat profile similar to the velocity in a turbulent single-phase flow. For all the other measured flow conditions, a similar trend for interfacial velocity is observed. However, at $y = 1$ mm, which is very close to the wall, the Group 2 bubble velocity has an unusual higher value than what is expected in this flow condition. This phenomenon may be possibly due to measurement error. It can also be observed that Group 2

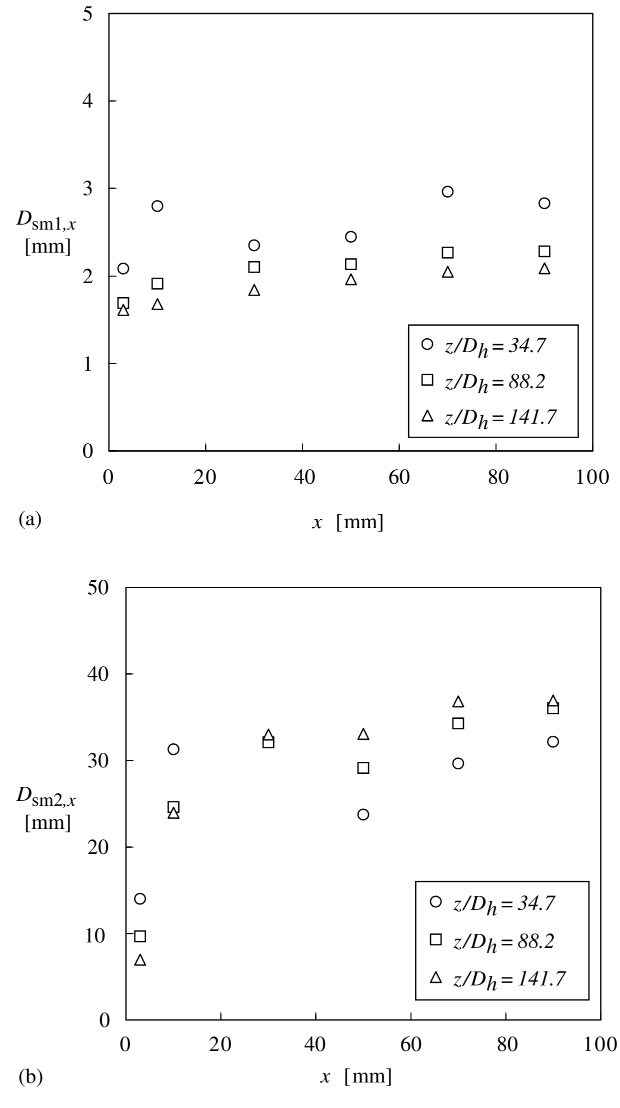

Fig. 8. y-Direction line-averaged Sauter mean diameter of (a) Group 1 and (b) Group 2 bubbles for Run 12 at three elevations.

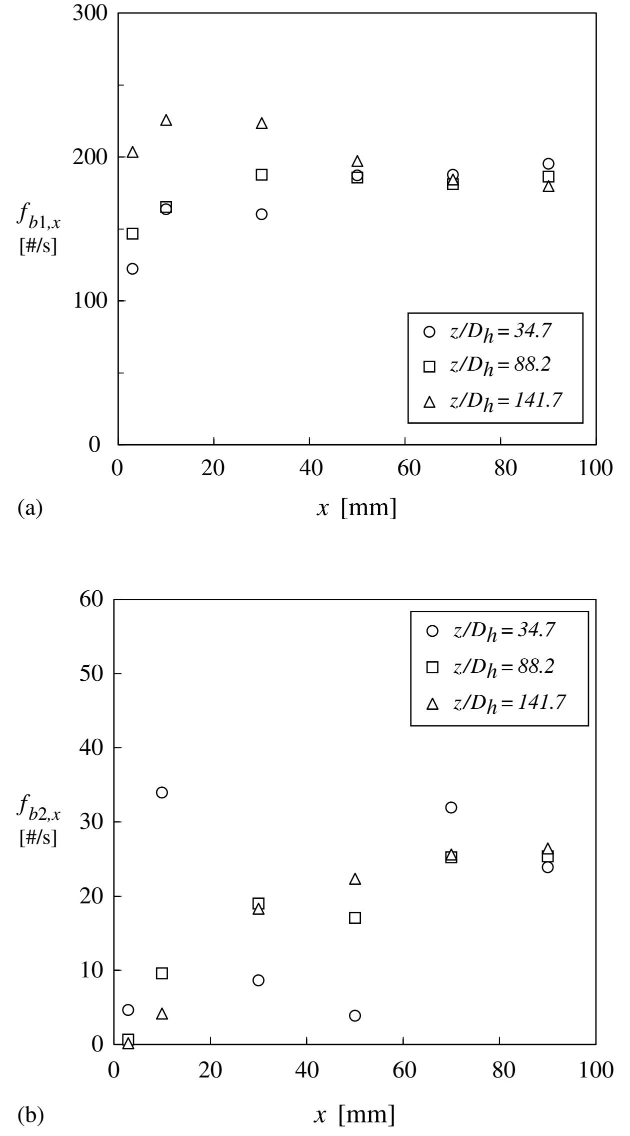

Fig. 9. y-Direction line-averaged bubble number frequency of (a) Group 1 and (b) Group 2 bubbles for Run 12 at three elevations.

bubbles have higher axial velocity compared to Group 1 bubbles at each measurement location. If one neglects the bubble deformation during the period of the penetration by the probe sensors, the axial interfacial velocity may be approximated as the average bubble axial velocity.

The distributions of the axial interfacial velocities in x-direction at $y = 5$ mm show a similar turbulent velocity profile, as indicated in Fig. 4(b). However, a strong entrance effect is observed at the lowest measurement port due to the inlet geometry of the current experimental loop. This phenomenon is also observed in the other flow conditions with high liquid flow rates. This is because when the liquid flow rates are high, liquid does not have enough time to "diffuse" and a "jet" is formed from each main liquid injection site. However, as the flow develops, the fluctuations gradually disappear. Kim et al. (2001a) also observed this phenomenon.

Fig. 5 displays the line-averaged axial interfacial velocities for both Group 1 and Group 2 bubbles for Run 12. Here, the line-averaged (over y-direction) axial interfacial velocity for Group 1 bubbles is computed as

$$v_{\mathrm{iz1},x} \equiv \frac{1}{G/2}\int_0^{G/2} v_{\mathrm{iz1}}(x,y)\,\mathrm{d}y. \tag{6}$$

The subscript x denotes the distribution along x-direction. The other line-averaged quantities are calculated in the same manner. It can be seen that, away from the wall, bubbles tend to move faster at a higher elevation. In this flow condition, the void-weighted area-averaged axial interfacial (bubble) velocity for Group 1 and Group 2 bubbles, i.e., $\ll v_{\mathrm{iz1}} \gg$ and $\ll v_{\mathrm{iz2}} \gg$, at z/D_{h} of 34.8, 88.2, and 141.7 are 3.85 and 4.35, 3.93 and 4.38, and 4.09 and 4.68 m/s, respectively. Here, the void-weighted area-averaged axial interfacial velocity is defined as

$$\ll v_{\mathrm{iz}k} \gg \equiv \frac{\int_A v_{\mathrm{iz}k}(x,y)\alpha_k(x,y)\,\mathrm{d}A}{\int_A \alpha_k(x,y)\,\mathrm{d}A} = \frac{\frac{1}{A}\int_A v_{\mathrm{iz}k}(x,y)\alpha_k(x,y)\,\mathrm{d}A}{\langle\alpha_k\rangle}, \tag{7}$$

where $k = 1$ and 2 for Group 1 and Group 2 bubbles, respectively; and $\langle\alpha_k\rangle$ is the area-averaged void fraction for Group k bubbles. The increase in the velocities is

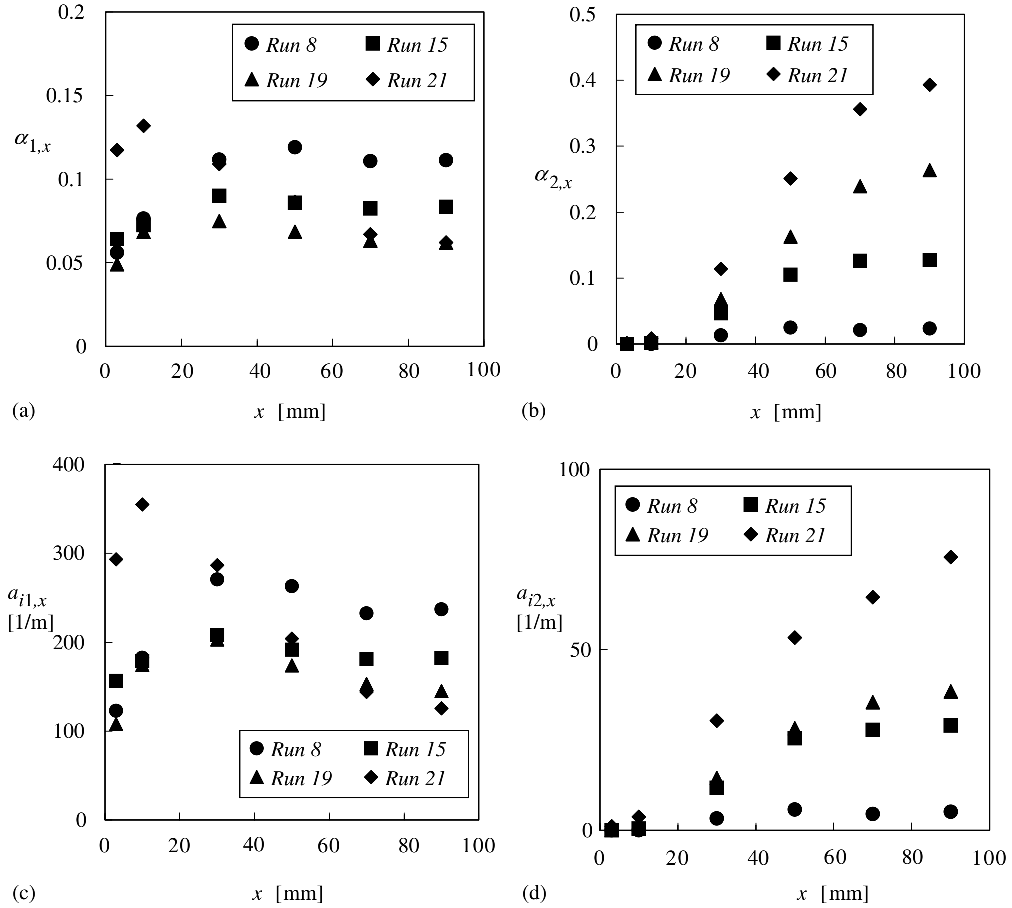

Fig. 10. Line-averaged (a) Group 1 and (b) Group 2 void fraction, and (c) Group 1 and (d) Group 2 interfacial area concentration for Runs 8, 15, 19, and 21 at $z/D_{\mathrm{h}} = 141.7$.

mainly due to the hydrodynamic effects since the pressure drop along the flow direction is comparable to the system pressure in the current atmospheric pressure condition. Certainly, for Group 2 bubbles, the larger size may also lead to a higher bubble velocity.

Furthermore, the line-averaged (over y-direction) void fraction, interfacial area concentration, Sauter mean diameter, and bubble number frequency for both Group 1 and Group 2 bubbles are presented in Figs. 6–9 for Run 12. For Group 1 bubbles, the void fraction in the center region of x-direction dramatically decreases along the flow direction because Group 1 bubbles coalesce to form Group 2 bubbles in this region, as shown in Fig. 6(a). For α_2, the entrance effect can be observed again. Nevertheless, α_2 slightly increases as the flow develops. Also, it has a larger value around the center region of x-direction and a relatively small value close to the wall at Port 4 and Port 6. This implies that the large bubbles tend to move to the center of the test section.

The interfacial area concentration has a physical meaning of the interfacial area per unit mixture volume. For Group 1 bubbles, a significant wall peak is observed, as shown in Fig. 7(a). This phenomenon is related to the bubble number frequency, bubble velocity, and bubble size. The Sauter mean diameter of Group 1 bubbles is quite uniform across the width of flow channel at Port 4 and Port 6, as indicated in Fig. 8(a). While for the bubble number frequency, there exist more Group 1 bubbles close to the wall region as shown in Fig. 9(a). The combination of these effects leads to the wall peak at the topmost measurement port. For Group 2 bubbles, the interfacial area concentration shows similar profiles as the void fraction.

The size of Group 1 bubbles decreases as the flow evolves for Run 12, as shown in Fig. 8(a). This decreasing trend might be a sign that the bubble disintegration is dominant instead of bubble coalescence at the region close to the wall of x-direction. In fact, this can be proved from the bubble number frequency as shown in Fig. 9(a). However, in the center region, Group 2 bubbles slightly grow along the flow direction due to the pressure effect as well as the coalescence between Group

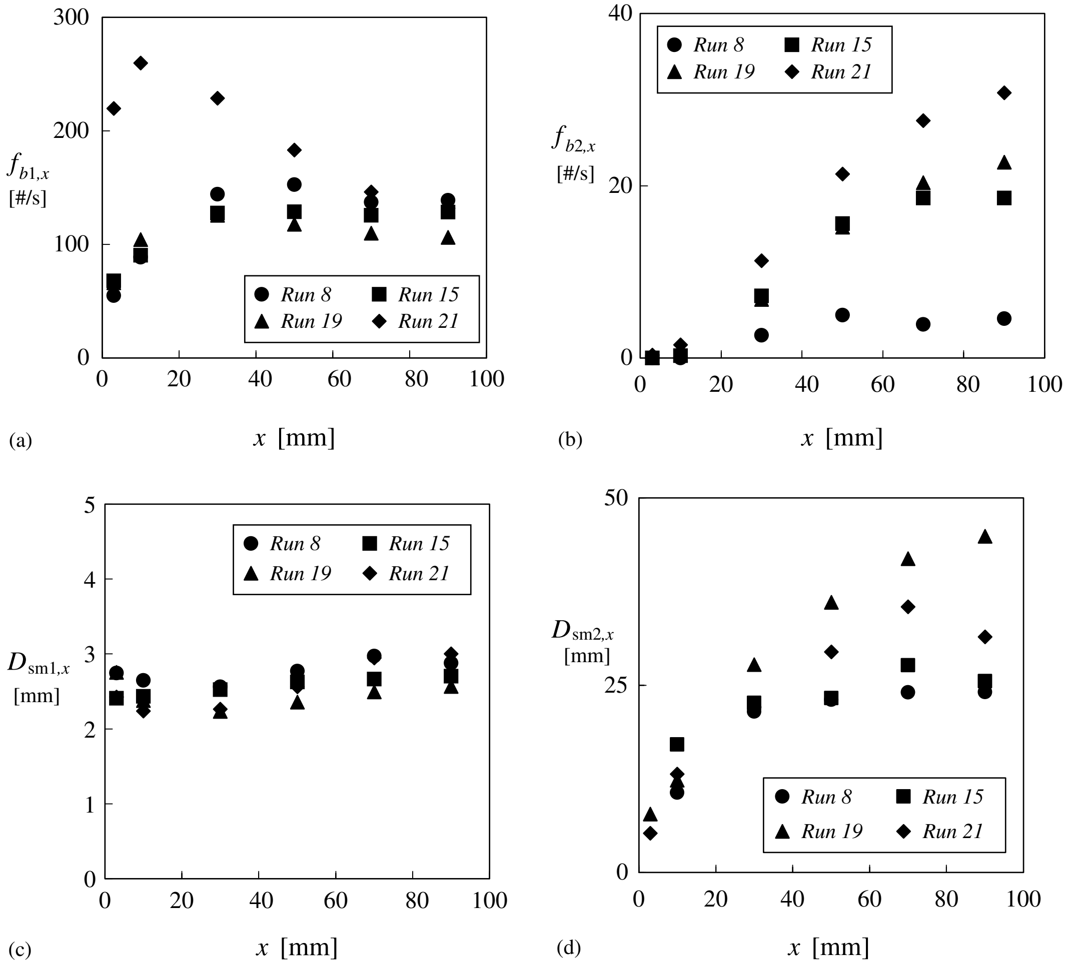

(a) (b)

(c) (d)

Fig. 11. Line-averaged (a) Group 1 and (b) Group 2 bubble number frequency, and (c) Group 1 and (d) Group 2 bubble Sauter mean diameter for Runs 8, 15, 19, and 21 at $z/D_h = 141.7$.

1 and Group 2 bubbles. Meanwhile, the slow increase of the Group 2 bubbles number frequency indicates the formation of Group 2 bubbles from the coalescence between Group 1 bubbles at the center region of flow channel.

In addition to the axial development of the flow structure, the comparisons also made between the different flow conditions at the same elevation. Figs. 10 and 11 are the line-averaged void fraction, interfacial area concentration, bubble number frequency, and bubble Sauter mean diameter for Runs 8, 15, 19 and 21 acquired at Port 6. In these flow conditions, the liquid flow rates are the same while the gas flow rates increase from Runs 8 to 21, as shown in Table 1. Run 8 is cap-turbulent flow while Run 15 is at the transition region from cap-turbulent to churn-turbulent flow. And the other two runs are in churn-turbulent flow regime.

The total void fraction increases with the increase of the gas flow rate, as expected. However, the void fraction for Group 1 bubbles becomes smaller from Run 8 to Run 15, and further to Run 19, and then increases from Run 19 to Run 21. Also, a wall peak profile is formed in Run 21, as shown in Fig. 10(a). On the other hand, Group 2 void fraction always increases with the increase of the gas flow rate. And Group 2 bubbles are more concentrated in the center region. In contrast to the total void fraction, the total interfacial area concentration decreases continuously from Run 8 to Run 19. However, it increases dramatically from Run 19 to 21. This shows that Group 1 bubble is the main contributor to the interfacial area concentration while Group 2 bubble becomes important to the void fraction with the increase of gas flow rate. Furthermore, Fig. 11(c) shows that the average size of Group 1 bubbles across the test section is quite uniform. It is interesting to note that the average Group 1 bubble size decreases from Run 8 to Run 19. However, the size of Group 2 bubbles continues to increase as the gas flow rate

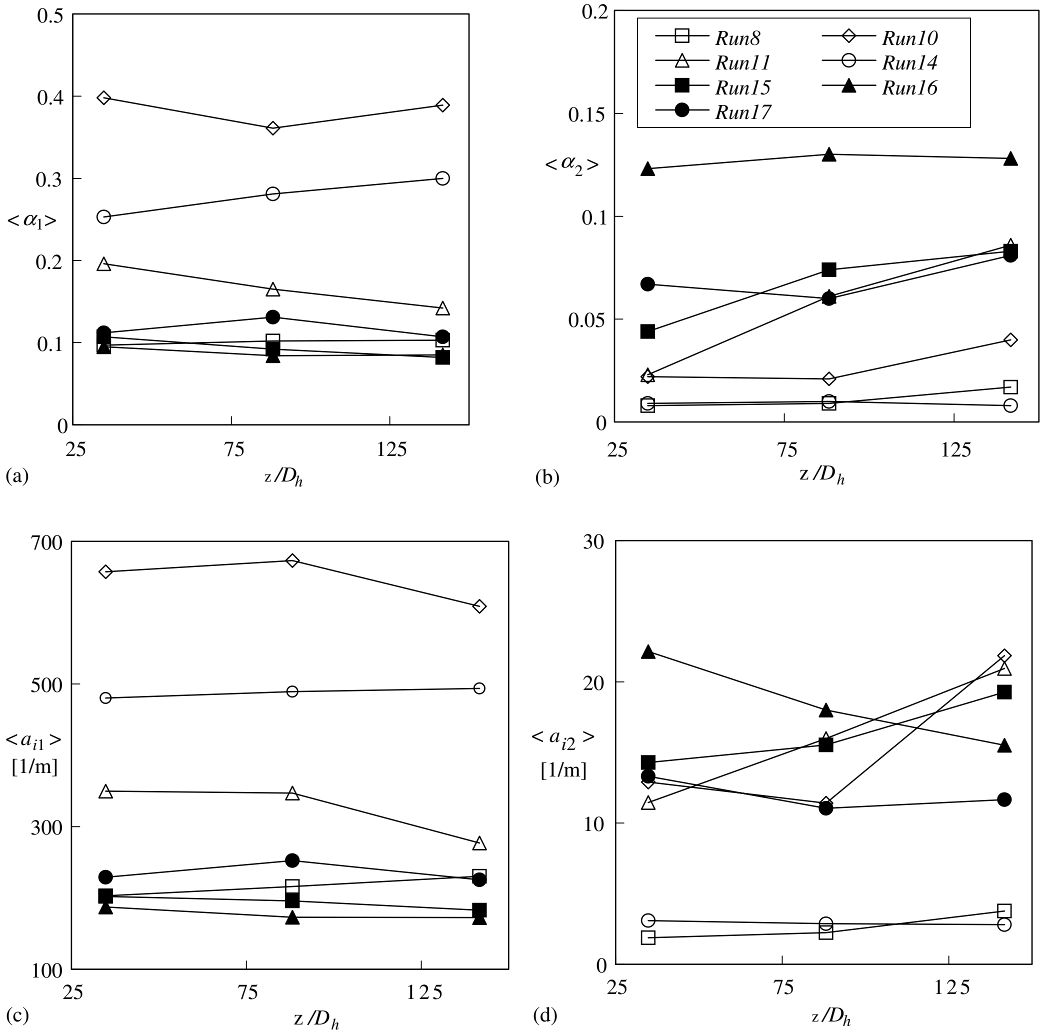

Fig. 12. Area-averaged (a) Group 1 and (b) Group 2 void fraction; (c) Group 1 and (d) Group 2 interfacial area concentrations in cap-turbulent flow at three elevations. (Refer to (b) for legend. Lines are only for better presentation.)

increases from Run 8 to 19, and then decreases from Run 19 to 21, as shown in Fig. 11(d).

The decrease in size and void fraction of Group 1 bubbles from Run 8 to 19 implies that the coalescence of Group 1 bubbles makes a significant contribution to inter-group transport of bubbles. On the other hand, the increase in size, void fraction, and bubble number frequency of Group 1 bubbles and the decreases in Group 2 bubbles size from Run 19 to 21 indicates that there are some mechanisms to generate small bubbles out of large bubbles. This could be the disintegration of Group 2 bubbles due to turbulence as well as the shearing off of smaller bubbles from Group 2 bubbles. It is evident that the inter-group transport of bubbles is a very dynamic and flow condition dependent process. It mainly involves fluid particle interactions. Furthermore, it is also interesting to note that the area-averaged void fractions for Runs 8 and 15 are less than 0.2, although they are already in cap-turbulent flow regime. This is mainly due to the geometry and size of the test section, as well as the unique liquid injection in this experimental loop.

Moreover, the axial development of the area-averaged void fraction and interfacial area concentration for both bubble groups are shown in Figs. 12 and 13. Fig. 12 is for cap-turbulent flow while Fig. 13 is for churn-turbulent flow. For $\langle\alpha_1\rangle$, Runs 11, 12, and 15 show a relatively large decrease along the flow direction. This implies that the effect of the inter-group transport from Group 1 to Group 2 bubbles due to Group 1 bubble coalescence is more significant compared to the pressure effect alone. However, in Run 14, $\langle\alpha_1\rangle$ has an increasing trend as the flow develops. This may be due to the fact that this flow condition is at the transition region from bubbly to cap-turbulent flow and inter-group transfer is not yet significant. Therefore, the bubble expansion due to the hydrodynamic effects dominates. Moreover, in Runs 18, 20, and 21, $\langle\alpha_1\rangle$ also increases in the flow direction, which is mainly because of the generation of

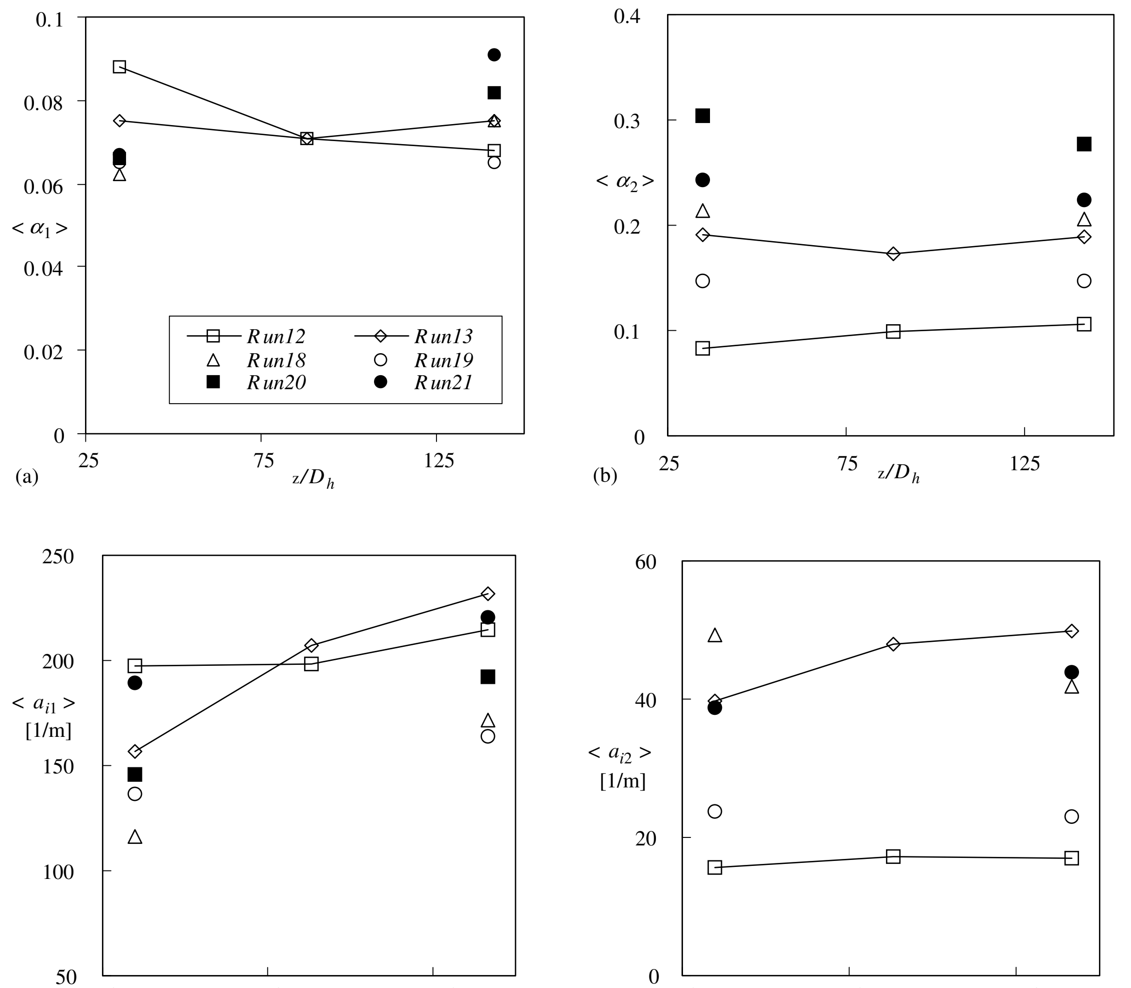

Fig. 13. Area-averaged (a) Group 1 and (b) Group 2 void fraction; (c) Group 1 and (d) Group 2 interfacial area concentrations in churn-turbulent flow at different elevations. (Refer to (a) for legend. Lines are only for better presentation.)

Group 1 bubbles from Group 2 bubbles. It is interesting to note that the void fraction of Group 1 bubbles can be as high as about 0.4 in Run 10 due to the relatively weak turbulence in the continuous phase, which does not promote bubble coalescence. On the other hand, $\langle \alpha_2 \rangle$ increases along the axial direction in most flow conditions except Runs 14, 19–21. For Run 14, this may be due to the increase of Group 2 bubble velocity. However, for Runs 19–21, due to the significant small bubble shearing-off mechanism and the increase of the bubble velocity for Group 2 bubbles, void fraction for Group 2 bubbles slightly decreases or remains almost constant along the flow direction.

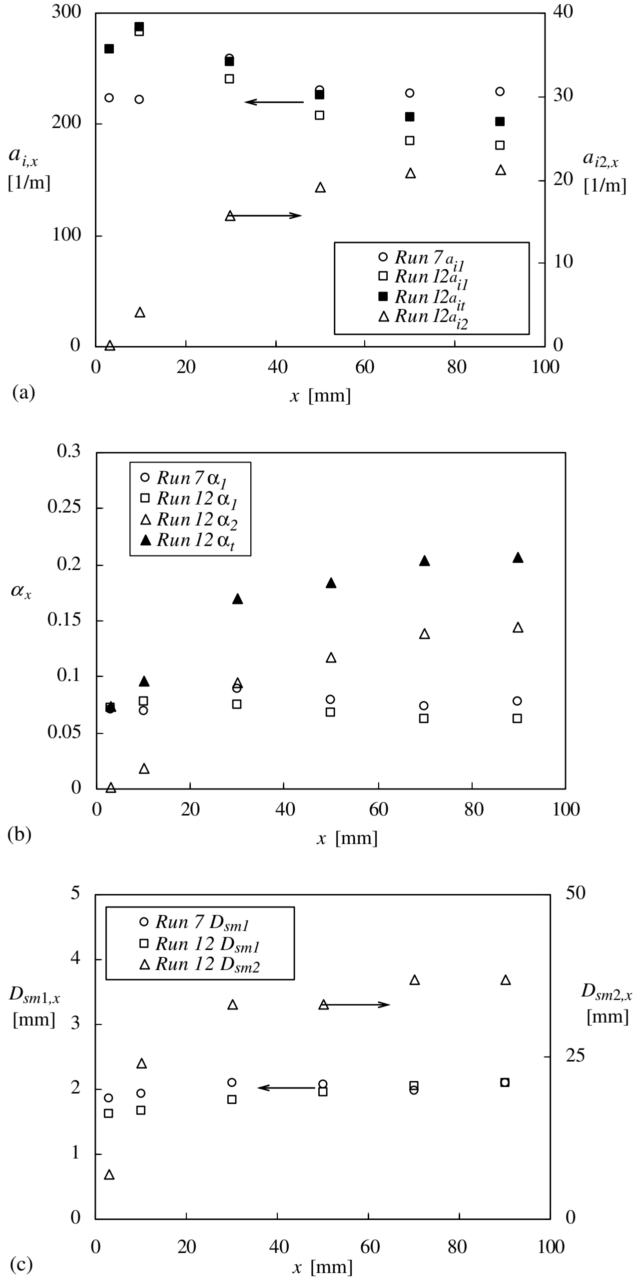

Fig. 14. Comparisons between Run 7 and Run 12 at $z/D_h = 141.7$ for (a) interfacial area concentration, (b) void fraction, and (c) bubble Sauter mean diameter.

Corresponding to the void fraction, the area-averaged interfacial area concentration for Group 1 bubbles, $\langle a_{i1} \rangle$, also show a decreasing trend along the axial direction for Runs 10, 11, 15, and 16. However, in Runs 12, 13, and 18–21, $\langle a_{i1} \rangle$ increases significantly as the flow develops due to the shearing-off of small Group 1 bubbles from large bubbles. In fact, the average size of Group 1 bubbles decreases in the flow direction in these flow conditions. On the other hand, $\langle a_{i2} \rangle$ exhibits similar features to the $\langle \alpha_2 \rangle$ except Run 13. In Run 13, there is a significant decrease for $\langle \alpha_2 \rangle$ while an increase is observed for $\langle a_{i2} \rangle$ at Port 4. Large increase of Group 2 bubble velocity at Port 4 might attribute to this phenomenon. In general, as the flow travels upward, more Group 2 bubbles are formed due to the inter-group transport from Group 1. A different phenomenon, however, may be worth noting. For Runs 20 and 21, $\langle a_{i2} \rangle$ increases while the number and size of Group 2 bubbles become smaller along the flow direction. This may be due to the fact that in the churn-turbulent flow conditions, the interface of Group 2 bubbles becomes very irregular and chaotic, which leads to more interfacial area for a Group 2 bubble with a certain size.

Finally, the current experimental results are compared to the previous work reported by Kim et al. (2001a), in which the air–water two-phase flow was restricted to the bubbly flow regime. In bubbly flow, no Group 2 bubbles were observed. In the current experiment, the interfacial area concentration is always dominated by Group 1 bubbles, although the void fraction for Group 2 bubbles could be significant compared to Group 1 bubbles. In other words, the interfacial area of small bubbles is more important in view of interfacial heat transfer. In addition, Group 2 bubbles always tend to migrate to the center region (in x-direction) of the test section; while Group 1 bubbles, in both churn-turbulent and bubbly flows, can have a wall-peaked distribution in terms of the void fraction and interfacial area concentration. In churn-turbulent flow, the motion and therefore the distribution of the small bubbles (Group 1 bubbles) are strongly affected by the large Group 2 bubbles. The liquid turbulence is noticeably enhanced by the motion of the Group 2 bubbles. The churn-turbulent bubbles are essentially two dimensional since the gap of the test section is 10 mm. As an example, the results from previous bubbly flow experiment, Run 7 ($j_{g0} = 0.30$ and $j_f = 2.84$ m/s), at $z/D_h = 141.7$ are compared with the current Run 12 experiment, as shown in Fig. 14.

5. Conclusions

The experiments in a total of 13 flow conditions at cap-turbulent and churn-turbulent flow regimes have been performed in a vertical air–water upward loop. The miniaturized four-sensor conductivity probes are used to measure local time-averaged interfacial velocity, void fraction, bubble number frequency, interfacial area concentration, and bubble Sauter mean diameter for both Group 1 and Group 2 bubbles. Due to the geometry of the present experimental loop, no slug flow regime is identified. Instead, the cap-turbulent and churn-turbulent flow may occur at smaller void fraction compared to the conventional round pipe. In general, Group 2 bubbles have a relatively larger velocity compared to Group 1 bubbles at the same location. Furthermore, Group 1 bubbles are the main contributors to the interfacial area concentration although the void fraction of Group 1 bubbles may be much less than that of Group 2 bubbles in certain flow conditions.

The experimental results demonstrate the development of the interfacial structure due to the bubble interactions and the hydrodynamic effects. In flow conditions of high liquid flow rate, bubble disintegration mechanism is more important than bubble coalescence in view of the inter-group bubble transport. In relatively low liquid flow rates, bubble coalescence can be considered as the major bubble interaction mechanism in cap-turbulent flow. However, the pressure effect is always important in the present study due to the atmospheric pressure experimental condition. The current data may serve as a part of the experimental data to investigate the interfacial area transport in a confined two-phase flow.

References

Fu, X.Y., 2001. Interfacial area measurement and transport modeling in air–water two-phase flow. Ph.D. Thesis, Purdue University, West Lafayette, IN.

Hewitt, G.F., 1978. Measurement of Two-Phase Flow Parameters. Academic Press, New York. pp. 120–125.

Ishii, M., 1975. Thermo-Fluid Dynamic Theory of Two-Phase Flow. Eyrolles, Paris. pp. 99–100.

Ishii, M., 1987. Interfacial area modeling. In: Hewitt, G.F., Delhaye, J.-M., Zuber, N. (Eds.), Multiphase Science and Technology, vol. 3. Hemisphere Publishing.

Kalkach-Navarro, S., Lahey Jr., R.T., Drew, D.A., Meyder, R., 1993. Interfacial area density, mean radius and number density measurements in bubbly two-phase flow. Nucl. Eng. Des. 142, 341–351.

Kataoka, I., Serizawa, A., 1990. Interfacial area concentration in bubbly flow. Nucl. Eng. Des. 120, 163–180.

Kataoka, I., Ishii, M., Serizawa, A., 1986. Local formulation and measurements of interfacial area concentration in two-phase flow. Int. J. Multiphase Flow 12, 505–529.

Kim, S., Fu, X.Y., Wang, X., Ishii, M., 2000. Development of the miniaturized four-sensor conductivity probe and the signal processing scheme. Int. J. Heat Mass Transfer 43, 4101–4118.

Kim, S., Sun, X., Ishii, M., Beus, S.G., 2001a. Development of gas–liquid two-phase flow interfacial structure in a confined bubbly flow. In: Proceedings of ICONE 9, Paper No.: ICONE-121.

Kim, S., Sun, X., Ishii, M., Lincoln, F., 2001b. Interfacial area transport in a confined bubbly flow. In: Proceedings of ICONE 9, Paper No.: ICONE-122.

Kocamustafaogullari, G., Ishii, M., 1995. Foundation of the interfacial area transport equation and its closure relations. Int. J. Heat Mass Transfer 38, 481–493.

Kocamustafaogullari, G., Ishii, M., Chen, I.Y., 1984. Unified theory for predicting maximum fluid particle size for drops and bubbles. NUREG/CR-4028, US Nuclear Regulatory Commission.

Kocamustafaogullari, G., Huang, W.D., Razi, J., 1994. Measurement and modeling of average void fraction, bubble size and interfacial area. Nucl. Eng. Des. 148, 437–453.

Mishima, K., Ishii, M., 1984. Flow regime transition criteria for upward two-phase flow in vertical tubes. Int. J. Heat Mass Transfer 27, 723–737.

Neal, L.G., Bankoff, S.G., 1963. A high resolution resistivity probe for determination of local void properties in gas–liquid flow. AIChE J. 9, 490–494.

Revankar, S.T., Ishii, M., 1992. Local interfacial area measurement in bubbly flow. Int. J. Heat Mass Transfer 35, 913–925.

Taitel, Y., Bornea, D., Dukler, A.E., 1980. Modelling flow pattern transitions for steady upward gas–liquid flow in vertical tubes. AIChE J. 26, 345–354.

Wu, Q., Ishii, M., Uhle, J., 1998a. Framework of two-group model for interfacial area transport in vertical two-phase flows. Trans. ANS 79, 351–352.

Wu, Q., Kim, S., Ishii, M., Beus, S.G, 1998b. One-group interfacial area transport in vertical bubbly flow. Int. J. Heat Mass Transfer 41, 1103–1112.